A critical examination of the influence of material characteristics and extruder geometry on 3D Printing of cementitious binders

Sooraj A.O. Nair[1], Subhashree Panda[2], Manu Santhanam[3], Gaurav Sant[4], and Narayanan Neithalath[5,*]

Abstract

Extrusion pressure-displacement tests on cementitious pastes with multiple starting materials and differing particle packing, subjected to different extrusion geometries are reported. The steady state extrusion pressure (equivalent to extrusion yield stress) and the deadzone length (static zone of material buildup at die entry) are determined from the pressure-displacement response to characterize the extrudability and/or printability. A unique "geometric ratio" is used to account for the effects of barrel-die geometry on paste extrusion. The ratio of extrusion yield stress (25-75 kPa) to the measured shear yield stress (50-300 Pa), the deadzone length, and the measured-to-designed filament volume at a given flow rate (print speed) are found to remain relatively invariant with geometric ratio for mixtures with high degree of microstructural packing, and thus better extrudability and shape stability. This paper marries materials- and process-related issues and, could pave the way for test methods for 3D printable mixture qualification.

Keywords:

3D printing; cementitious binders; extrusion; geometric ratio; dead zone

[1] Graduate student, School of Sustainable Engineering and the Built Environment, Arizona State University, Tempe AZ 85287

[2] Visiting Graduate student, School of Sustainable Engineering and the Built Environment, Arizona State University, Tempe AZ 85287 (Graduate Student, Vellore Institute of Technology, India)

[3] Professor, Department of Civil Engineering, Indian Institute of Technology Madras, India

[4] Professor and Henri Samueli Fellow, Department of Civil and Environmental Engineering, University of California Los Angeles, Los Angeles CA

[5] Professor, School of Sustainable Engineering and the Built Environment, Arizona State University, Tempe AZ 85287; [*]Corresponding author; Narayanan.Neithalath@asu.edu; Phone: +1-480-965-6023; Fax: +1-480-965-0557

1 Introduction

3D printing (additive manufacturing), a ubiquitous method in the fabrication of ceramic, automotive and aerospace components, has garnered the attention of the construction industry in the recent past [1–5]. Researchers are attempting to take advantage of: (i) shape and topology optimization, (ii) reducing wastage of materials, and (iii) integration of building information modeling (BIM) that are facilitated by 3D printing techniques, to ensure the creation of next generation of sustainable and efficient structures. Small scale buildings have portrayed the potential of 3D printing as a faster and optimal mode of construction [6–8]. Layered extrusion, where the binder is extruded through a nozzle layer-by-layer is the most common 3D printing technique for cementitious materials [9–11] while other methods such as powder printing [12,13] have also been studied.

The extrusion response of the printed material is crucial in 3D-printing a layered system with the desired performance characteristics. The type of extrusion process, the process parameters including extrusion speed, extruder geometry, layer height and width, and the material properties influence the quality of the printed component in terms of structural stability and finish [14]. It is well accepted that cementitious systems are disordered solid-liquid assemblies (suspensions) whose flow behavior exhibits several complex phenomena such as yield stress behavior, thixotropy, and time-and-pressure dependence [15]. The rheological properties need to be tailored to satisfy conflicting requirements including extrudability, flowability, buildability, layer stability, and retention time [16–18]. Recent research has identified significant material characteristics that influence layer-wise extrusion and printing under different process conditions, which has led to preliminary guidelines for mixture composition [13,15,19–22].

As mentioned earlier, the properties of an extruded and 3D printed cementitious element depends on the material and process characteristics, necessitating their combined use to predict and control the print output. Minor changes in formulation or operating conditions can lead to flow instabilities and product defects [23], e.g., liquid phase migration. The fundamental parameters in extrusion include the extensional yield stress (also termed as extrusion yield stress, which is used throughout this paper), die wall shear stresses, and the length of static material deposition (dead zone) in the barrel at the die entry. The constrictivity of the barrel-to-die entry influences the extrusion yield stresses [24,25]. Also, the pressure drop across the die is generally linearly dependent on the length-to-diameter ratio of the die, which is widely used in estimating the die wall shear stresses. The extrusion process relies on the extrusion system overcoming the resistance of the paste and maintaining the required flow rate, while ensuring a defect free extrudate with requisite buildability. In this paper, the extrusion pressure-ram displacement

relationships for a series of cementitious pastes are used to analyze the critical materials-and-process related parameters of relevance. This paper introduces a unique dimensionless geometric factor that accurately captures the influence of extruder geometry on the rotational and extrusional rheological parameters of importance with respect to cementitious paste extrusion. Moreover, the combined effect of material properties and the extrusion geometry on deadzone formation, that influences the extrusion process and the print quality, is brought out. The experiments are carried out on a set of multiple-material cementitious binder systems with different initial particle size distributions and packing. The geometric ratio which relates to the extruder geometry is ultimately related to a flow ratio, which is an indicator of the influence of the material characteristics on the print quality. The approach described in this paper can be tailored towards the development of test methods and analysis procedures to determine the combined influence of materials and geometry on extrusion-based 3D printing.

2 Characterization of cementitious paste extrusion

In paste extrusion, the material (both extrudate and barrel/die) characteristics, extrusion geometry, and the imposed stress states on the extrudate are critical parameters that determine the efficiency of the process and the quality of the extrudate. Ram extrusion is generally carried out using barrel-die or orifice configurations. The extrudate parameters that govern the extrusion process can be broadly classified as being functions of the rheological characteristics of the fresh paste, i.e., yield stress and plastic viscosity. For a simple barrel-die geometry, the barrel diameter (D), die entry diameter (d_{entry}), die exit diameter (d_{exit}), length of the barrel filled by the material (L_0), and length of the die (L_{die}) are the crucial geometry-related parameters (See Figure 1(a)). The extrudate-barrel/die friction also influences the extrusion process, along with the extrusion rate, that in turn influences the degree of consolidation of the paste while extruding. Extrusion models used to predict the force of extrusion under ram extrusion [26–31] generally identify two steps during the extrusion process: first, the initial compaction or pre-consolidation of the material in the geometry (Step I in Figure 1(b)), and second, the actual extrusion of the material [26]. However, for cementitious materials, which can be considered as two-phase (solid-liquid) media, the actual extrusion phase has been reported to constitute plastic deformation (Step II in Figure 1(b)), which is sometimes followed by a radial flow regime that results in a pressure rise (Step III in Figure 1(b)) [25]. Step III is a measure of the retentive cohesion of the mixture under pressure, which is influenced by the 'dead zone', which is a static zone formed at the bottom of the barrel when the material is forced under pressure. The material does not move in this zone, and it forms the outer shell for extrusion near the die entry.

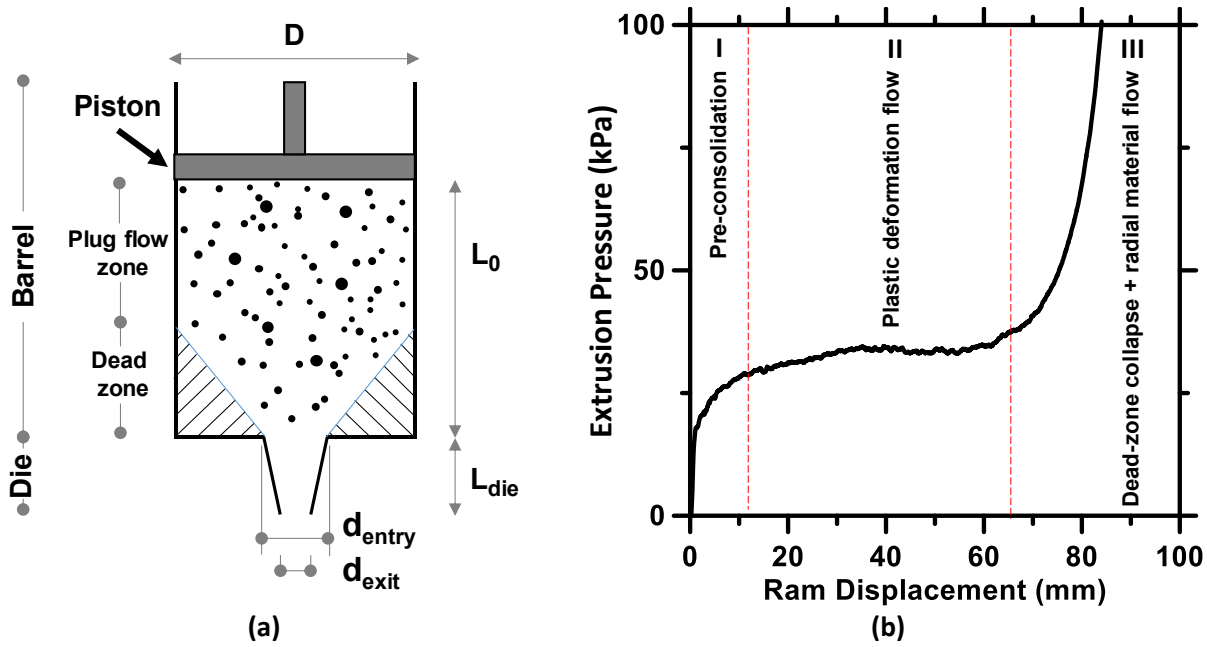

Figure 1: (a) A typical barrel-die system, and (b) steps in ram extrusion of a cementitious material

3 Experimental Program

3.1 Materials and mixtures

Ordinary portland cement (OPC) conforming to ASTM C 150, a class F fly ash conforming to ASTM C 618, microsilica (silica fume) conforming to ASTM C 1240 and fine limestone powder conforming to ASTM C 568 were used to proportion the pastes. The chemical compositions of the starting materials are shown in Table 1 and their particle size distributions in Figure 2. The paste mixture proportions used in this study along with the packing fraction (φ) and degree of microstructural packing (φ/d_{50}^2) [22]) are given in Table 2. The mixture proportions were selected such that the pastes were uniformly and homogeneously extruded through different die geometries. Note that the pastes have different water-to-powder ratios (w/p) since the objective is to ensure extrudability, which varies as a function of the particle sizes and their distribution in the paste. For example, a pure OPC paste was extrudable and more-or-less printable (see discussions later for detailed description of these) at a w/p of 0.32, but when limestone powder of mean particle size 1.5 μm replaced 30% by mass of cement, a w/p of 0.41 was needed to ensure extrudability and printability.

Table 1: Chemical composition of the paste components

Components of the binders	Chemical composition (% by mass)						
	SiO_2	Al_2O_3	Fe_2O_3	CaO	MgO	SO_3	LOI*
OPC	19.60	4.09	3.39	63.21	3.37	3.17	2.54
Fly ash (F)	58.40	23.80	4.19	7.32	1.11	3.04	2.13
Micro silica (M)	> 90.0	-	-	< 1.0	-	-	-
Limestone (L), 1.5 µm	$CaCO_3$ > 99%						

*Loss on ignition

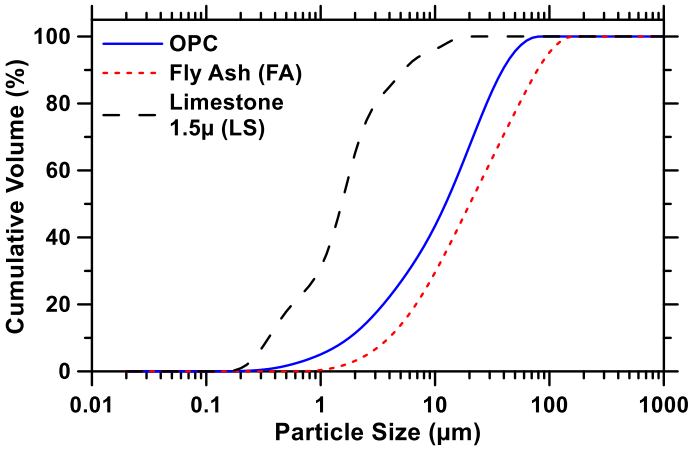

Figure 2: Particle size distribution of constituent materials. The PSD of microsilica is not shown, but the median size is $< 0.5\ \mu m$ in a well-dispersed state.

Table 2: Mixture proportions used for the experiments

Mixture ID	Mass fraction of ingredients				Water-to-powder ratio (w/p), by mass	Super-plasticizer (% by mass of powder)	Solid volume fraction (φ)	Micro-structural index [22] (φ/d_{50}^2), x 10^3 µm^{-2}
	OPC	Fly ash (F)	Limestone (L); d_{50} = 1.5 µm	Micro-silica (M)				
OPC	1.0	0	0	0	0.32	0	0.403	2.64
F_{30}	0.70	0.30	0	0	0.30	0	0.439	2.12
L_{30}	0.70	0	0.30	0	0.41	0	0.324	9.92
$L_{15}M_{15}$	0.70	0	0.15	0.15	0.445	0	0.301	13.83
L_{30}-s	0.70	0	0.30	0	0.35	0.25	0.382	11.71

3.2 Rheological characterization

The yield stress and plastic viscosity of the paste mixtures used in this study were evaluated using a dynamic shear rheometer (TA instruments AR2000EX) in a parallel plate geometry. The 50 mm diameter serrated Peltier plate geometry was conditioned to a temperature of 25 ± 1°C with a gap of 2 mm. The

upper and lower plates had groove depths of 1 mm and 0.15 mm respectively to avoid paste slip. The pastes were subjected to strain rates between 0.1 and 100 s^{-1} [32,33], to determine the Bingham yield stress and plastic viscosity. The test procedure includes: (i) a stepped ramp-up pre-shear to homogenize the paste for 75 s, (ii) stepped ramp-up shear, and (iii) stepped ramp-down shear. The shear stress versus strain rate data at each ramp step was recorded at the rate of 2 data points per second using TA Instruments' TRIOS software. The apparent shear stress and plastic viscosity were extracted from the down-ramp data. More information on the experimental process can be found elsewhere [32,34].

3.3 Single speed extrusion tests

The extrusion cell used in this study had a cylindrical barrel of 36 mm in diameter and a length of 100 mm and holds 100 cm^3 of cement paste. The details of the die and/or orifice geometries are shown in Table 3. The extrusion cell was placed under a 4.45 kN MTS universal testing machine to extrude the material under a displacement rate-controlled regime, at a constant ram displacement rate of 25 mm/min. The test was stopped when the total displacement reached ~100 mm, or when the pressure required to extrude the material caused noticeable changes in extrudate quality.

Table 3: Different die geometries used in extrusion studies

Designation and details of die geometries		[redacted]				[redacted]
		Orifice		Uniform die		Tapered die
Designation		O10	O4	N10-10	N4-4	N10-4
Entry diameter, d_{entry}	(mm)	10	4	10	4	10
Exit diameter, d_{exit}	(mm)	-	-	10	4	4
Length of die, L	(mm)	0	0	36	36	36
L/d_{exit}	-	0	0	3.6	9	9

The entry and exit diameters of the die largely determines the extrusion characteristics with respect to the extruder geometry. The nomenclature for the geometries in Table 3 shows the type of configuration (O - Orifice and N - Nozzle or die) followed by the pair of die entry and exit diameters (i.e. 10-10 means a uniform diameter of 10 mm while 10-4 means a die tapering from 10 mm to 4 mm). Note that the entry and exit is at the same point in the case of an orifice and the barrel diameter of 36 mm is consistent across the geometries tested.

3.4 3D printing of the paste and dimensional analysis

The paste mixtures and geometries described earlier were subjected to extrusion in a BCN3D+ model paste extrusion 3D printer. Hollow cubes, 50 mm in side length were first printed to evaluate the printability of the mixtures using an N10-4 geometry at a print speed (or nozzle travel speed) of 22.2 mm/s. For dimensional analysis of the printed filaments, the extruder geometries shown in Table 3 were used along with a print speed that corresponds to a fixed ram speed of 25 mm/min used in the extrusion test. The print speed required to generate a filament of given dimensions were calculated using the die exit flow rate and Bernoulli's continuity equation. Table 4 shows the print parameters including the layer dimensions and the calculated print speed. The cross-sectional dimensions of the filament were selected based on a previous study on 3D printable pastes where the filament width was set as $1.5d_{exit}$ and height as $0.75d_{exit}$ [22]. These values are chosen as an extreme case scenario where the layer height is close to the nozzle diameter and the layer width is twice the layer height. Filaments were printed and the post-print quality was evaluated from multiple measurements of the printed filament dimensions.

Table 4: Print parameters for the extruded mixtures in equivalent 3D printing

Cross-section (C/S)		**N10-10**	**N10-4**	**N4-4**
Layer Width (LW)	mm	15	6	6
Layer Height (LH)	mm	7.5	3	3
Print speed	mm/s	3.56	22.2	22.2
Flow rate	mm^3/s	400		

4 Results and Discussion

4.1 Shear yield stress and plastic viscosity of the pastes

Figure 3 shows the rotational rheological parameters of the mixtures shown in Table 2. Note that the w/p is different for the mixtures because the aim was to obtain smooth, extrudable pastes (see [22] for more details on these pastes). The L_{30}-s mixture that contains limestone and proportioned with a lower w/p than the L_{30} mixture showed the highest shear yield stress (see the following discussion the microstructural index). The presence of superplasticizer enhances particle dispersion even at high solid concentrations. The $L_{15}M_{15}$ mixture showed a relatively higher yield stress as compared to the L_{30} mixture which can be attributed to the presence of microsilica in the former case that again increases the number of interparticle contacts. The OPC paste demonstrated the lowest yield strength among the mixtures studied, due to its coarser particle size distribution and consequently, a lower microstructural index shown

in Table 2. The F_{30} paste shows a higher yield stress and plastic viscosity than the OPC paste because of the lower w/p used for the fly ash modified paste. However, the F_{30} mixture showed similar yield stresses and a higher plastic viscosity as compared to the limestone modified mixtures, even at a lower w/p ratio. This can be partly attributed to the lower water retention capacity of the OPC and F_{30} pastes due to the lower specific surface area (i.e., larger particle sizes) and the weak van der waal's force of attraction between the particles [33]. Companion studies at a higher w/p for the F_{30} mixture (comparable to the OPC mixture) did show a significant reduction in yield stress and plastic viscosity, as expected. The ultrafine limestone lends a cohesive nature to the mixture, and along with increased packing density, reduction in the inter particle distance and capability to retain water, provides for adequate printability [22,33,35].

Microstructural packing effects are important in ensuring sufficient yield stress for the particle network in the fresh state, which enables printability. It has been shown that the suspension yield stress can be taken to be proportional to the solid volume fraction and inversely proportional to the square of median particle size (i.e., $\tau \propto \phi/d_{50}^2$) [22,36,37]. This parameter has been shown to scale well with a microstructural factor that employs the number density, coordination number and mean centroidal distance from virtual microstructures of cementitious suspensions [22]. Table 2 provides the values of ϕ/d_{50}^2 for the pastes evaluated in this work as a quantifier of their microstructural packing

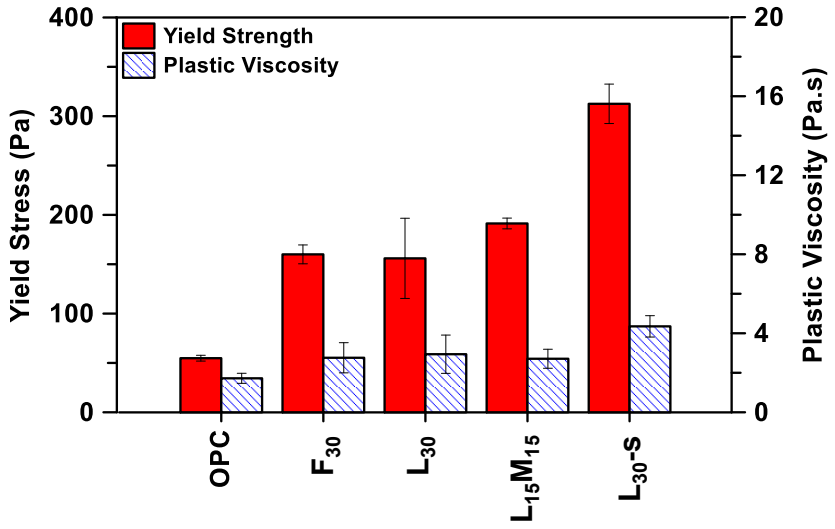

Figure 3: Shear yield stress and plastic viscosity of the selected paste mixtures

4.2 Extrudability and extrusion characteristics of selected pastes

4.2.1 A geometric ratio for extrusion

The experimental studies were carried out on different barrel-die geometries shown in Table 3. The configuration of the exit geometry influences the pressure required to shape the material out of the barrel, as well as the temporal and spatial evolution of total force required to extrude the material. Extrusion ratio, which is the ratio of the opening diameter (d_{entry}) to the barrel diameter (D) is used in standard extrusion literature to quantify this effect [38]. However, an orifice configuration will require only a lower pressure to extrude than a uniform die system because of the absence of friction in the die. Also, a tapered die provides a higher resistance because of the increased die surface area as compared to one with a uniform diameter. Hence, to quantify the influence of the die geometry, a geometric ratio (Ψ) is developed in this study. It is based on the die length-to-diameter ratio and the constrictivity of the entrance from the barrel to the die. ψ is defined here as:

$$\psi = \frac{(D - d_{entry})}{d_{entry}} \left(1 + \sqrt{\frac{4L}{d_{exit}}} \right) \qquad \text{Eq. 1}$$

The constrictivity is quantified based on the radial strain (the first term in Eq.1), and the effect of die wall friction is accounted for by a term that uses the ratio of surface area of the die to the cross-sectional area of the die exit. This value, $4L/d_{exit}$ for uniform dies (i.e., $d_{exit} = d_{entry}$), can be found in other established formulations such as the Benbow-Bridgwater equation [24]. In the case of tapered die, the $4L/d_{exit}$ term is replaced by the ratio of the actual die surface area to its exit cross-sectional area. Thus, the $4L/d_{exit}$ term in this equation is only applicable for a uniform die and needs to be modified appropriately for different die shapes. The formulation assumes the die entry diameter to be lower than the barrel diameter; in cases where they are the same (i.e., tapering die starts at the barrel end itself), the average constrictivity between the die entry and the exit can be considered. Table 5 shows the geometric ratios for different geometries used in this study. Higher the geometric ratio, harder it is to extrude the paste through the geometry.

Note that, in the formulation shown in Eq. 1, if a die is present, the constrictivity is enhanced by a multiplier equal to $1 + \sqrt{\frac{4L}{d_{exit}}}$ as compared to the orifice case. Experiments have shown that the major contributor to the total extrusion pressure is the shaping stress between the barrel and the constriction (called the die entry pressure), and the die land pressure (the frictional effect as the paste passes through

the die) is a smaller contributor. However, this effect is dependent on the paste characteristics as well as L and d_{exit} values. Using the Benbow-Bridgwater model for extrusion pressure measurements [22] and Bagley correction [39], it was determined that the ratios of die entry pressure to die land pressure (k) vary between 0.10 to 0.30 for the pastes without superplasticizer and ~0.05 for the paste with superplasticizer for the mixtures shown in Table 2. Therefore, the parameter in the parenthesis in Equation 1 could be restated as $1 + k\sqrt{\frac{4L}{d_{exit}}}$. This modification will account for the effect of the material also on the geometric ratio. However, the determination of such a geometric ratio will need extrusion experiments *apriori*, leading to less ease-of-use. As an example, for N10-10 geometry, ψ= 12.5 when the material effect is not considered (see Table 5), ψ= 3.1 for $L_{30\text{-}s}$ mixture, and ψ= 6.25 (4 mm d_{exit}) and 3.4 (8 mm d_{exit}) for L_{30} mixture. In order to avoid laboriousness in calculations, the geometric ratio is simplified in this paper and stated as just the effect of barrel-die geometry. This formulation leaves open, the choice of incorporating the material characteristics through further experiments, if desired.

Table 5: Different die geometries used in extrusion studies

Geometry designation	O10	O4	N10-10	N4-4	N10-4
Geometric ratio (ψ)	2.6	8.0	12.5	56	23.4

4.2.2 Extrusion characteristics and their implications

Figure 4 shows a typical extrusion pressure - ram displacement data. The rapid increase in pressure at the beginning of the test indicates initial consolidation. During the second step, i.e., steady state extrusion, the material is capable of continuously flowing through the opening at a relatively constant pressure. Further consolidation during the steady state condition and the occurrence of water filtration (if any) could result in a slight increase in stress during this stage as can be noticed in some of the extrusion curves. However, this effect is assumed to be limited and the steady state flow continues until the plug flow zone is completely extruded. The average pressure between ram displacements of ~20 to 60 mm is calculated and reported as the steady state pressure in this study. The third step which indicates a disproportionate effort to extrude the paste, can be noticed by plotting the curvature of the pressure-displacement relationship, as shown in Figure 4. The deadzone length is defined as the distance from the point of maximum curvature to the die entry as shown in this figure.

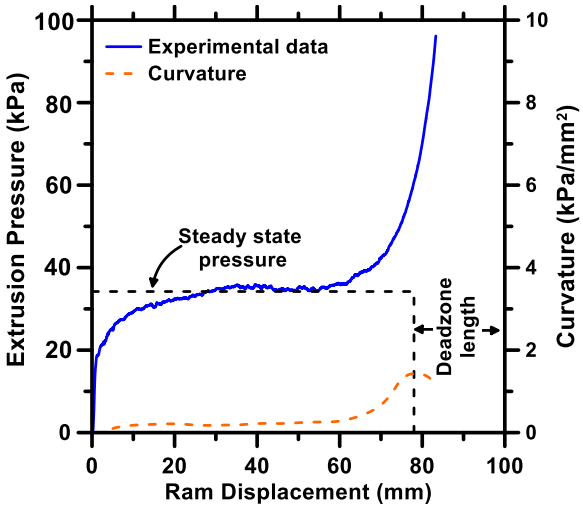

Figure 4: A typical single velocity extrusion data of OPC in O10 configuration showing the average steady state pressure and deadzone length

The extrusion pressure – ram displacement for the different pastes are shown in Figure 5. The results when a plain OPC paste was extruded at a constant velocity are shown in Figure 5(a) for different extruder geometries. The general order of steady state extrusion pressure is found to be: N4-4 > N10-4 > N10-10 > O4 > O10. The steady state extrusion pressure is found to increase with the geometric ratio (ψ) of the configurations. The orifice geometry O10 (10 mm opening) requires the least extrusion pressure when compared to other configurations. O4 (4 mm orifice opening) geometry shows a higher extrusion pressure than the O10 geometry since the force required to shape the material through a smaller exit diameter (to maintain the same flow rate) is higher. The introduction of die significantly alters the extrusion pressure since the geometric ratio changes. N4-4 geometry (4 mm uniform die) shows a higher extrusion pressure than the N10-10 (10 mm uniform die) geometry. The influence of die on the total pressure is non-negligible since the material must overcome the die wall friction to exit the system. The shaped material entering the die has a different particle organization than that in the barrel because of the shaping stress that it has been subjected to, when moving from the barrel to the die. The additional packing effect and the frictional stresses exerted by the material on the wall depend on the w/p and particle organization in the mixture [22]. Figure 5 and Table 6 also show that the ram displacement at which extrusion pressure exponentially increases (which is an indicator of deadzone lengths, elucidated later in this paper), reduces when the geometric ratio (ψ) is increased. The plug flow zone length reduces and the deadzone length increases under high pressures, especially at lower extrusion velocities [40]. This effect is more prominent at higher barrel diameter-to-die entry ratios [41], which increases ψ as can be seen from Eq. 1.

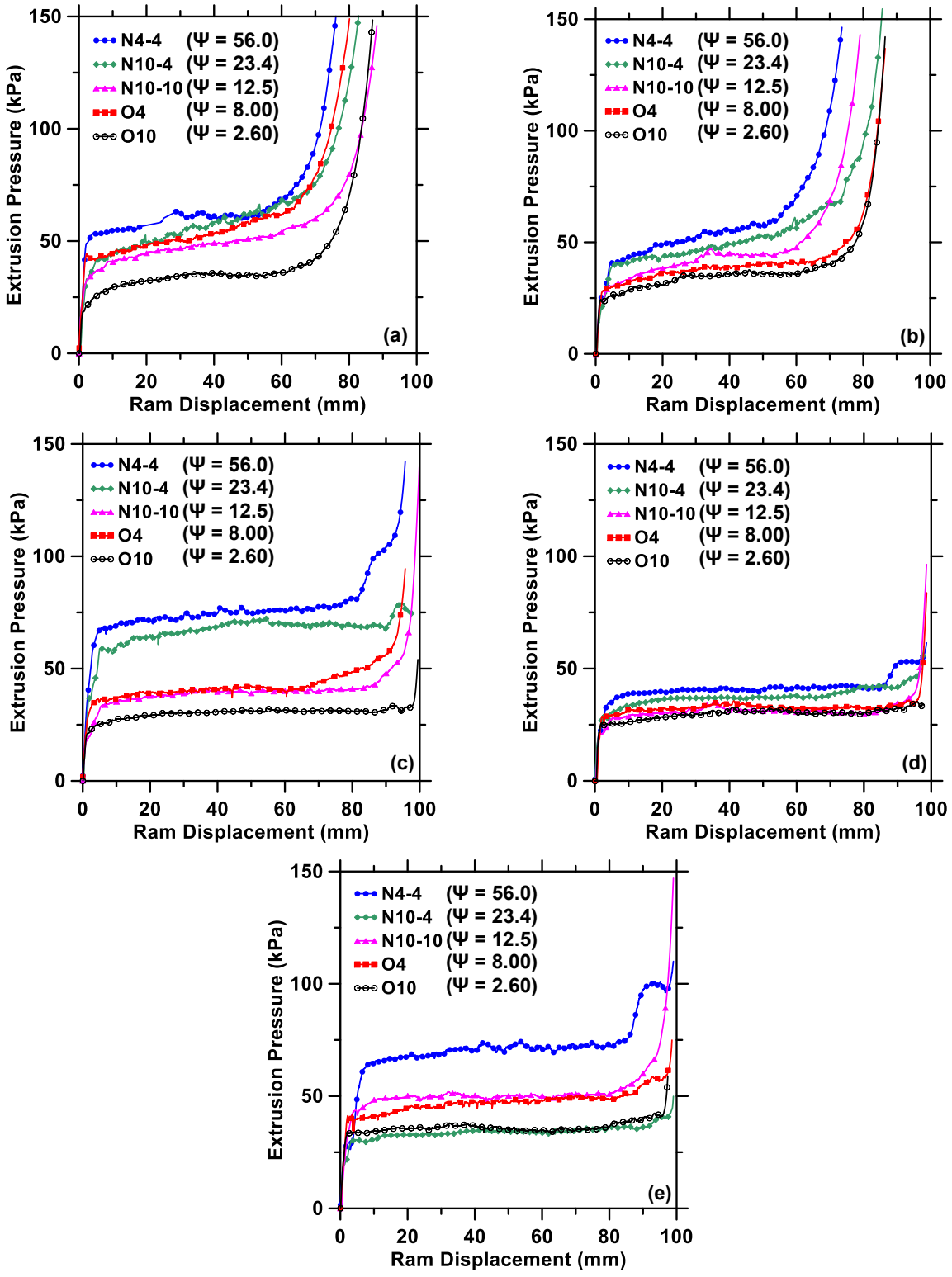

Figure 5: Extrusion pressure - displacement relationships recorded for different geometries for the different pastes: (a) OPC, (b) F_{30}, (c) L_{30}, (d) $L_{15}M_{15}$, and (e) L_{30}-s

Figures 5 (b)-(e) depict the extrusion pressure – displacement response for the pastes containing cement replacement materials. From Figures 5(a) and (b), it can be noticed that the OPC and F_{30} pastes show rapid increase in extrusion pressure (origin of Step III) at a relatively early ram displacement (61-78 mm) when compared to the other mixtures. This can be attributed to the inadequate particle packing characteristics in these mixtures [22]. When the microstructural packing is tailored through the addition of fine particles such as limestone powder and silica fume, Step III occurs at a much later ram displacement (around 86-96 mm) as can be noticed from Figures 5(c)-(e). In other words, the dead zone length for such mixtures is less than 15 mm. Even though the barrel wall frictional force reduces with increasing ram displacement (because the contact area between the paste and the barrel wall reduces with increasing ram displacement), the pressure required for extrusion increases in the dead zone because of the effects of consolidation and water filtration. For mixtures with carefully controlled microstructural packing and beneficial rheology, the dead zone length is much lower. Incidentally, these mixtures demonstrate desirable extrudability and printability, as shown in the next section. The fact that most of the material in the barrel extrudes without the need for extreme pressure indicates beneficial overall particle organization within the paste and its cohesiveness. The dead zone length and its relationship with ψ are discussed later in this paper.

Table 6: Ram displacement value at the point of exponential increase in extrusion pressure

Geometry	Geometric ratio (ψ)	Point of exponential in pressure rise (mm)				
		OPC	F_{30}	L_{30}	$L_{15}M_{15}$	L_{30}-s
O10	2.6	78	76.5	96.5	96	95
O4	8	71.5	61	91.5	89.5	91
N10-10	12.5	70.5	65.9	91.8	90	93
N10-4	23.4	67	75.5	88	92	88
N4-4	56	68.5	66	86.5	92	87

4.2.3 Printability of the selected pastes

The selected mixtures were evaluated for printability using an N10-4 geometry at a print speed of 22.2 mm/s. A hollow cuboid of 45 mm x 45 mm x 30 mm in size was printed with a filament height and width of 3 mm and 6 mm respectively. Figure 6 shows the printed cuboids using the different mixtures. The OPC and F_{30} mixtures were extrudable initially but not buildable as evident from Figures 6(a) and (b) which shows filaments slumped when stacked in layers or the extrusion process being discontinuous as more paste is extruded from the barrel, because of changes in the paste flow due to consolidation and water filtration under hydrodynamic conditions. For the given printer-controlled-extruder system and print parameters, the OPC paste specifically demonstrated difficulties in maintaining the flow rate and showed

discontinuities as can be noticed from this figure. The irregular filament widths resulted in local stress concentrations and incremental shifts in the filament position. Hence, the overall specimen is distorted and fails by slumping. The F_{30} paste was relatively consistent in flow owing to the spherical fly ash particles that enable easy flowability. However, the water retention was poor and liquid filtration caused filament stability issues with layer build up. Figure 6(b) shows how the print deformed at the top due to the overburden pressure on the relatively weaker lower filaments. Figures 6(c)-(e) shows the printable limestone-containing pastes which are buildable when compared to the extrudable, yet non-buildable OPC and F_{30} pastes. The printed layers were able to be stacked without local failure or slumping. The individual layer stability (owing to the thixotropy) and the overall buildability (owing to the relatively high yield stress of the paste within the printable zone [18,42]) generated consistent layers with less defects and a better finish. This is on account of the extrudate quality and the consistent flow of material for the chosen geometry that contributes to individual layer stability. This is evaluated for different geometries and discussed in a forthcoming section.

(a) OPC **(b) F_{30}** **(c) L_{30}**

(d) $L_{15}M_{15}$ **(e) L_{30}-s**

Figure 6: 3D printed cuboids to evaluate buildability for the selected paste mixtures

4.3 Extrusion stresses as a function of composition and extrusion geometry

The average steady state stress (σ_{ss}) from extrusion experiments is an indicator of the stress required to shape the paste from the barrel to the die after pre-consolidation. Thus, this easily measurable value can be used as a proxy for the extrusion yield stress of the material when it just starts moving through the orifice or the die entry. Note that the extrusion yield stress is different from the shear yield stress that is commonly measured in the pristine state, and that it is not a material property since it is influenced by the extruder geometry. The extrusion yield stress has also been related sometimes to a compressional or squeeze yield stress since the extrusion process can be considered to be mechanistically similar to a squeeze flow case [43,44]. Thus, the effects of consolidation and the constraint imposed by the extruder geometry on the material response during extrusion is built into this parameter. The observed values of σ_{ss} lie in the 25-to-70 kPa range whereas the shear yield stresses prior to extrusion was in the 50-to-300 Pa range. The orifice extrusion pressures correspond to pure shaping without any die-effects and are in the range of 25-45 kPa. This is in line with earlier studies where extrusional yield stresses of 3-40 kPa were obtained for systems that demonstrated a consolidation-free shear yield stress of 50-200 Pa [45]. As noticed from Figure 5, there is a small increase in the pressure with further ram displacement even after the material is shaped into the die. This can be attributed to the non-zero barrel and die wall friction as well as internal particle rearrangements occurring in the paste even after being shaped into the die.

The steady state stresses are plotted in Figure 7(a) as a function of the geometric ratio for the pastes evaluated in this work. As expected, a generally increasing trend of shaping stress with the geometric ratio is observed. This is because of the higher stress required to maintain the plastic flow of the paste through the constriction [38]. For geometries with reduced resistance to flow (e.g., O10 with a $\psi = 2.6$), the steady state pressures are rather invariant of the mixture composition, while there is a distinct influence of the material on the steady state stress at higher geometric ratios. The steady state stresses also tend to plateau out at higher geometric ratios. This could be related to the length of dead zone formed at higher geometric ratios. It is conceivable that, for a given paste, the dead zone length also plateaus after a certain threshold constrictivity of the extruder geometry.

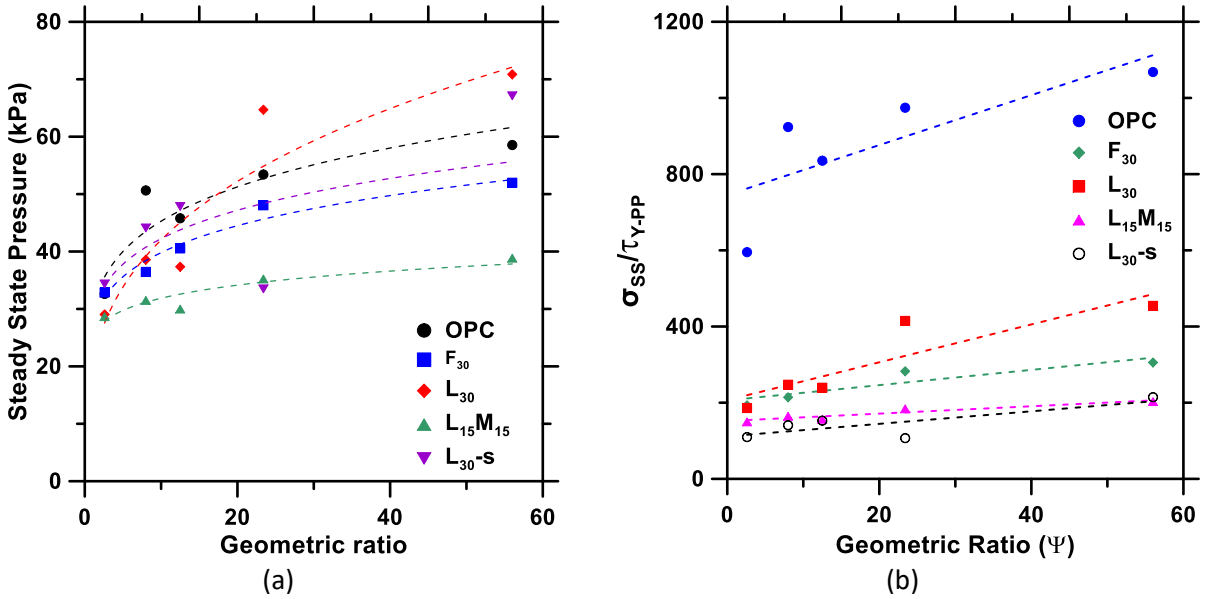

Figure 7: Relationship between geometric ratio (ψ): (a) steady state pressure with geometric ratio, and (b) ratio of predicted extrusion yield stress to experimental rotational shear yield stress.

A careful observation of Figure 7(a) shows that the order of steady state stresses of the pastes is different at different geometric ratios. This has to do with the fact that the geometric ratio, in reality, is different for different pastes based on the ratios of steady state stress to the die wall stress, which is a function of the material composition (or microstructural index), as explained in the section on formulation of ψ. However, as explained earlier, the material effects are ignored for simplicity, but can be added into the geometric ratio through additional extrusion experiments and analysis. To partly mitigate this difficulty and to better elucidate the influence of the paste characteristics on extrusion stress, Figure 7(b) plots the ratio of the average steady state stress (σ_{SS}) to the shear yield stress determined from parallel plate rheology experiments ($\tau_{Y\text{-}PP}$ from Figure 3; used here since it is the most commonly measured rheological parameter of cementitious suspensions) as a function of the geometric ratio. This ratio also places the extrusion stress in the context of shear yield stress, which is generally considered to be an independent material characteristic. The extrusion yield stress is 100-400 times higher (depending on the extruder geometry and based on the orifice extrusion) than the shear yield stress (ignoring the plain OPC paste that exhibited significant water filtration during extrusion and a longer dead zone – see Figures 5(a) and 6(a)).

The slope of the fit lines in Figure 7(b) indicates the degree to which the geometry is influential the extrudability of the paste. While for the plain OPC paste, increasing geometric ratio enhances the extrusion stress as compared to the shear yield stress by a factor of ~800-to-1000, the corresponding

enhancement is only by a factor of ~100-to-200 for the superplasticized mixture with limestone powder or the one containing limestone powder and microsilica. One implication of this ratio being less dependent on the geometric ratio is that such mixtures can be considered to be more robust for extrusion-based printing purposes since their reliance on extrusion geometry (within limits) is minimal. These mixtures demonstrated enhanced microstructural packing (see Table 2), which has been shown to be a desirable criterion for efficient extrusion and printing [22]. Hence, a combination of extrusion rheology and conventional parallel plate (or rotational) rheology can be a useful tool to evaluate the combined effect of materials and geometry on the effectiveness of cementitious blends for extrusion-based 3D printing.

4.4 Dead zone lengths in paste extrusion: A simple mixture qualification criterion

The dead zone length in paste extrusion is reported to dynamically change with the severity of liquid phase migration that is profound at lower extrusion velocities [40]. It also depends on the angle of repose of the material (< 55^o for cohesive and flowable mixtures), and the geometry of the barrel-to-die interface [46]. Predicting the deadzone length or shape could be an optimization problem [47,47,48]. However, this paper uses single speed extrusion tests as well as a combination of extrusion and rotational rheology to characterize and qualify extrudable mixtures for 3D printing. For ideal extrusion, the dead zone length has to be minimal; in other words, the entire mixture should be extrudable through a chosen barrel-die combination without the need for excess pressure. Excess pressure application detrimentally alters the characteristics of the printed material. The increase in length of the dead zone in the barrel can be attributed to different mechanisms as shown in Figure 8.

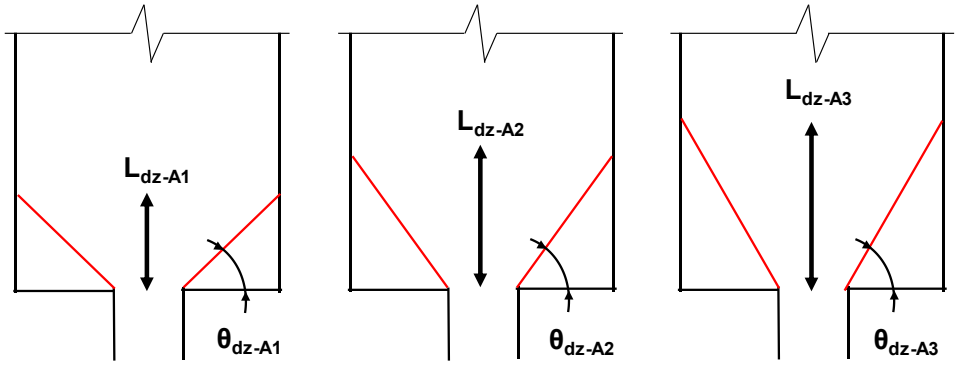

(a) Mechanism A: $\theta_{dz-A1} < \theta_{dz-A2} < \theta_{dz-A3}$ and $L_{dz-A1} < L_{dz-A2} < L_{dz-A3}$

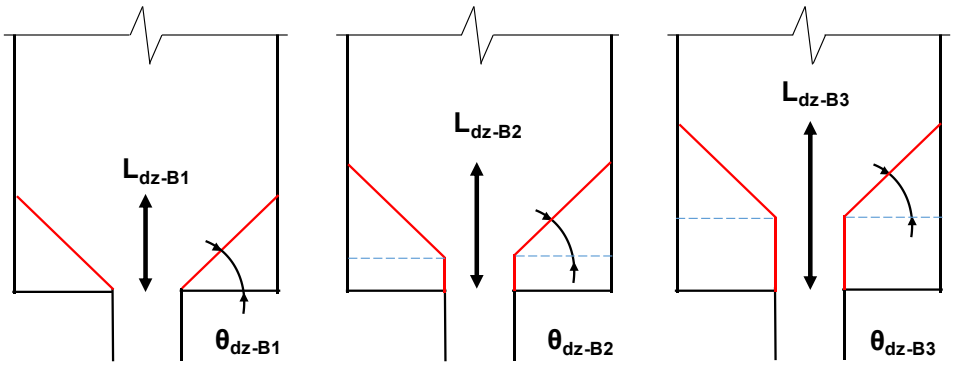

(b) Mechanism B: $\theta_{dz-B1} \approx \theta_{dz-B2} \approx \theta_{dz-B3}$ and $L_{dz-B1} < L_{dz-B2} < L_{dz-B3}$

Figure 8: Schematic showing mechanisms of dynamically changing deadzone length when: (a) dead zone angle increases, and (b) static zone length increases

Note that an increase in dead zone length results in barrel-paste frictional forces also being activated in that zone. In the first mechanism shown in Figure 8(a), generally reported in metal billet extrusion [38], the material near the surface undergoes substantial shear deformation as compared to the material in the center, with the angle θ_{dz} depending on the ratio of barrel cross-sectional area to the area of extrusion. As the extrusion area in the barrel decreases, θ_{dz} increases, and the length of the shear line also subsequently increases. In the second mechanism shown in Figure 8(b), a static zone of drained material is built up near the die entry as extrusion progresses. The angle of repose remains relatively constant while the overall length of the dead zone increases. The dead zone angle varies with changes in material properties because of secondary consolidation. Figure 9(a) shows the picture of a typical extruder after extrusion of a plain OPC paste and Figure 9(b) shows a close-up of the remnant material (deadzone) formed at the bottom of the extruder. Figure 9(c) shows a sectional view (section Z-Z) of the barrel interior showing the deadzone region formed, and a schematic of the isometric view as observed in the barrel is shown in Figure 9(d). The inclined region (denoted shaping zone) extends roughly halfway towards the die entry and then opens into the die with a constant diameter (denoted static zone). This is in conformance with the second mechanism. For cohesive, printable mixtures, exemplified by improved microstructural packing [22] (also see Figure 6), this length was found to be lower (see Table 6) and collapses when the piston reaches the deadzone region, and the flow ensues.

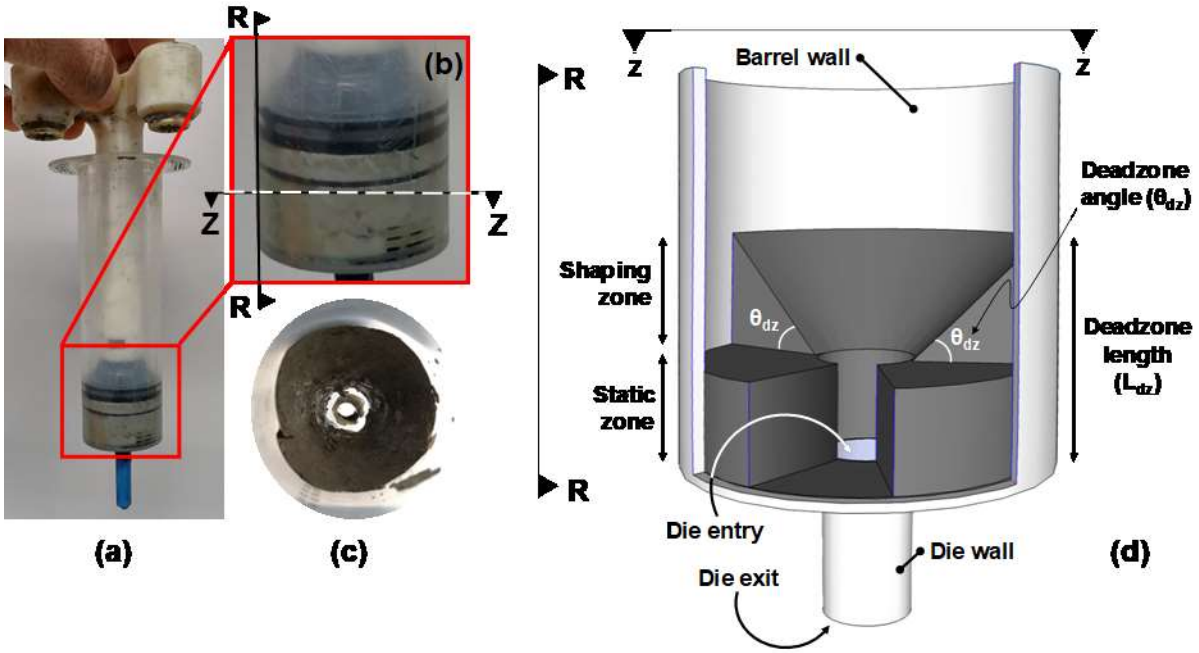

Figure 9: Typical dead zone formation under extrusion in a barrel-die system showing: (a) a typical extruder after the test, (b) zoomed in view of the extruder end showing the deadzone formed, (c) plan view from the top of the barrel, and (d) schematic of the dead zone angle and static zone (isometric view)

Deadzone length can be a useful, indirect indicator of the printability of the mixtures since a longer deadzone invariably results in difficulties in extrusion, wastage of material, and inhomogeneous print quality. Thus, it is desirable for printable mixtures to demonstrate shorter deadzone lengths and longer plug flow zones. The length of the deadzone has been estimated based on the point where the curvature of the pressure-ram displacement curve is the maximum, and physical observations of the deadzone (similar to those shown in Figure 9) has confirmed that this approach is accurate.

Figure 10(a) shows the deadzone lengths determined for all the five mixtures studied here, for all the extrusion geometries. It is easily seen that the plain OPC and OPC-fly ash pastes show deadzone lengths ranging from 20 to 40 mm, which is 20-40% of the length of the barrel. It is clearly noted that these pastes are less efficient in extrusion, and it is thus unsurprising that their printability was compromised, as shown in Figure 6 [22]. The inefficient packing and concomitant issues such as water filtration resulted in inhomogeneous extrudate and reduced shape stability. The dead zone lengths for the extrudable and printable mixtures were generally below 15 mm. As discussed earlier, better microstructural packing and the improved cohesion through the use of cement replacement materials enable reduced dead zone lengths. It can also be observed from this figure that dead zone lengths generally increase with increasing geometric ratio (or constriction).

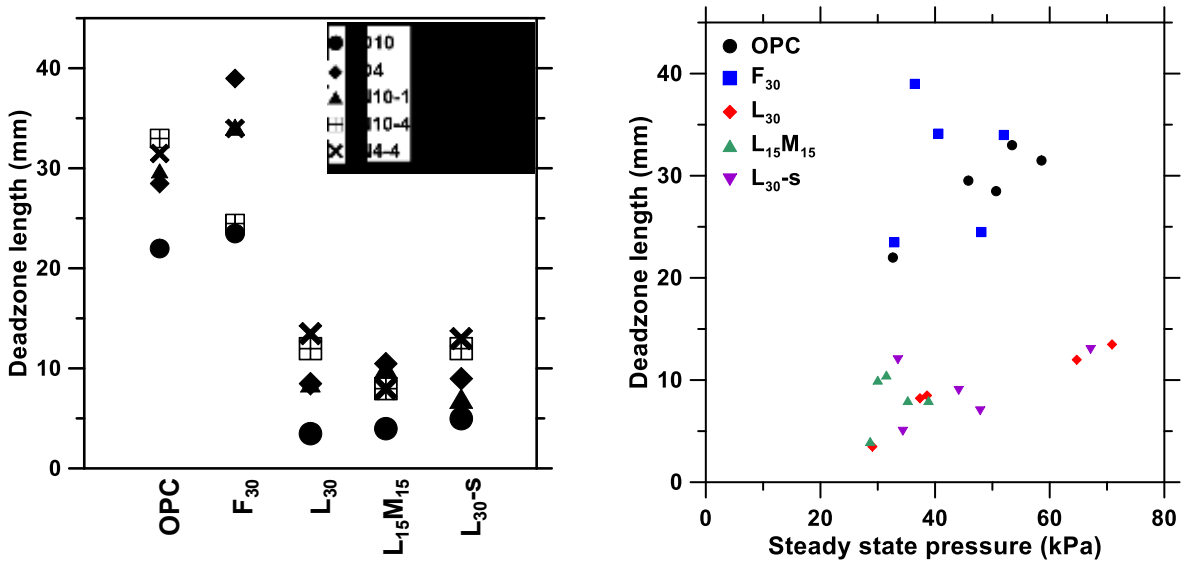

Figure 10: (a) Dead zone length of cementitious pastes extruded through different geometries, and (b) relative increase in deadzone length with steady state stress

It is rational to expect that the deadzone length will also be a function of the applied stress required to shape the material into the die. In general, the more the shaping stress required, the higher will be the chances of detrimental effects such as water filtration, especially when the overall porosity and the interparticle spacing in the mixture are higher. Figure 10(b) shows the variation of deadzone lengths as a function of the steady state stress (indicative of shaping stress) for the different mixtures and geometries used in this study. Since the steady state stress is a function of the extruder geometry, the influence of geometry is also accounted for in this figure. The non-printable mixtures show higher deadzone lengths for similar steady state stresses, for reasons described earlier. A significant observation from this figure is the relative invariance of deadzone lengths with respect to steady state stress for the printable mixtures. This further emphasizes the role of microstructural packing in ensuring robustness of the mixtures by which the effects of extruder geometry are minimized.

4.5 Filament 3D printing and print quality assessment using a flow ratio

While Figure 6 provided a qualitative evaluation of printability (including buildability), this section quantifies the influence of the material characteristics and geometric ratio along with the printing speed (for a fixed ram speed) on the dimensional accuracy of the printed filament. The designed filament dimensions, print speeds, and geometry are provided in Table 4. Typical printed filaments are shown in Figure 11(a) and (b). Using the print width and height, a flow ratio is defined, which is the ratio of the printed nominal cross-sectional area (based on average measurements at different locations shown in

Figure 11(a)) to the designed cross-sectional area. This ratio is a measure of the deviation from the designed flow rate assigned to the printer for a given geometry and material and is closely related to solidity ratio described in [49]. The ratio of cross-sectional areas is also quite similar to the shape retention factor (ratio of printed-to-designed layer width) used elsewhere for print quality determination [50]. However, the use of cross sectional dimensions to obtain the area (instead of just the width) makes the measurement more robust. It is possible that, for a given print speed, the printed width could deviate significantly when there are minor inconsistencies in the input height (or the z-correction in the printer). Large deviations of the flow ratio from 1.0 indicates inaccuracies in the extrusion/printing process, as is described below.

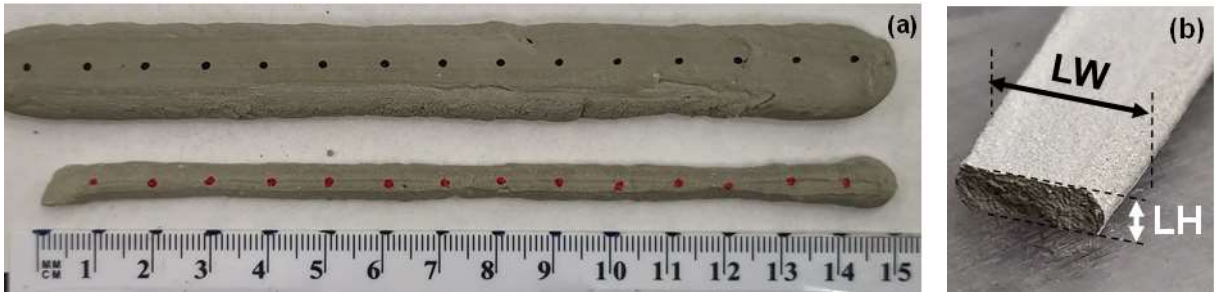

Figure 11: (a) Printed filaments using 10 mm (top) and 4 mm (bottom) diameter nozzles with points indicated on the filament for measurement of the actual cross-section dimensions, and (b) typical filament cross-section showing measured layer height (LH) and layer width (LW)

Figure 12(a) shows the flow ratios plotted as a function of the geometric ratio for all the chosen mixtures, while Figure 12(b) shows the statistical variability in the measurements. For the OPC and F_{30} pastes, the flow ratio is observed to drop with increasing geometric ratio. A lower flow ratio implies that the material is not extruded enough under the assigned conditions, resulting in smaller cross-sectional dimensions as compared to the designed values. In other words, as the constriction in the geometry increases, the paste undergoes significant changes and the printer is able to deliver only a reduced amount of material at the given print speed. The pastes with improved microstructural packing demonstrates mean flow ratios very close to 1.0, and they remain invariant with the geometric ratio. This observation is in line with the steady state stresses and deadzone lengths described earlier. In general, the variability in the measurements is higher when the geometric ratio is higher, as noticed from Figure 12(b). This indicates higher probability of uneven print filaments under constrained geometries in extrusion, with a potential to affect the layer stability and eventually the buildability.

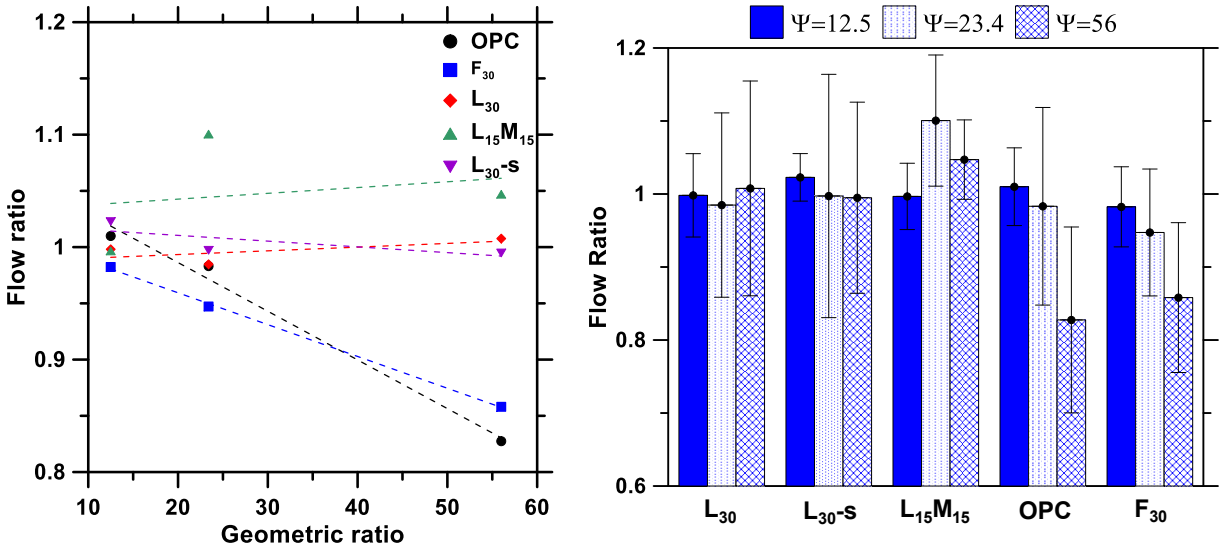

(a) (b)

Figure 12: (a) Mean values of flow ratio as a function of the geometric ratio for different pastes, and (b) variability in the flow ratio data for the different pastes

5 Summary and Conclusions

This paper has discussed the influence of material characteristics and extruder geometry on extrusion-based 3D printing of cementitious binders. Cementitious pastes (extrudable/extrudable-and-printable) containing multiple cement replacement materials including fine limestone and silica fume were used along with five different extrusion geometries. A unique geometric ratio (ψ) was developed to quantify the effects of geometry on the extrusion characteristics of the pastes. The geometric ratio explicitly accounts for the radial strain as the paste is constricted into the die and the effect of die wall geometry. An approach to incorporate the effects of the paste characteristics on the geometric ratio was also elucidated. The reported results were obtained from a limited set of cementitious pastes, print geometry, and printing parameters; however, the approach can be extended to a broader range of materials and printing parameters, provided further experiments are carried out.

Extrusion pressure-ram displacement relationships were used to determine the steady state pressure and the deadzone lengths. Such an approach was noted to provide a simple but efficient means of characterizing the extrudability of cementitious pastes. The steady state pressure was noted to increase with an increase in the geometric ratio, indicating the influence of geometric constriction on the extrusion pressure. The steady state pressures can also be related to the energy required for extrusion-based printing, thus helping in the design of appropriate extrusion-based printing systems. The steady state pressure was also shown to be an indicator of the extrusion yield stress. For the pastes used in this study

with shear yield stresses in the range of 50-to-300 Pa, the steady state pressures were in the 25-to-70 kPa range. The relationship between the geometric ratio and the ratio between the steady state pressure and shear yield stress was also used as an indicator of the combined influence of material and geometry on the printability of the pastes. For the mixtures that exhibited adequate particle packing and printability, the stress ratio was found to be less dependent on the geometric ratio, attesting to the robustness of the printable mixtures. Similarly, the deadzone length was shown to be an indirect, but easily measurable indicator of the printability of the mixtures, since a longer deadzone is more likely to create issues in extrusion and result in inhomogeneous print quality.

Filaments of predetermined dimensions were 3D printed using the different mixtures and different geometries at different printing speeds (i.e., flow rates) to determine a flow ratio (i.e., the ratio of the measured filament cross-sectional area to the designed cross-sectional area). The printable pastes demonstrated a rather invariant flow ratio with the geometric ratio, whereas the mean flow ratio significantly reduced with increasing geometric ratio for the non-printable mixtures, showing the impact of geometric constraints and the consequent changes experienced by such pastes while being extruded through such geometries. The geometric ratio was shown to be a useful parameter in this paper, which related well to several aspects of extrudability and printability of pastes. It needs to be emphasized that the proposed geometric ratio is limited to ram extruder systems, even though the concept could likely be directly extended to screw extruders as well. The geometric ratio and the approach described here could enable the development of test methods and protocols to evaluate the combined influence of paste materials and geometry on extrusion-based 3D printing.

6 Acknowledgments

The authors sincerely acknowledge support from U.S. National Science Foundation (CMMI: 1727445) and the Science and Engineering Research Board (SERB) of Govt. of India (through a VAJRA award to the last author) towards the conduct of this study. The contents of this paper reflect the views of the authors who are responsible for the facts and accuracy of the data presented herein, and do not necessarily reflect the views and policies of NSF, nor do the contents constitute a standard, specification or a regulation. We acknowledge the use of 3D printing and material characterization facilities within Laboratory for the Science of Sustainable Infrastructural Materials (LS-SIM) at Arizona State University.

7 References

1. Gosselin C, Duballet R, Roux Ph, Gaudillière N, Dirrenberger J, Morel Ph. Large-scale 3D printing of ultra-high performance concrete – a new processing route for architects and builders. Mater Des. 2016 Jun 15;100(Supplement C):102–9.

2. Hager I, Golonka A, Putanowicz R. 3D Printing of Buildings and Building Components as the Future of Sustainable Construction? Procedia Eng. 2016 Jan 1;151:292–9.

3. Scott C. 3D Printhuset Breaks Ground on 3D Printed Building in Copenhagen [Internet]. 3DPrint.com | The Voice of 3D Printing / Additive Manufacturing. 2017 [cited 2018 Apr 9]. Available from: https://3dprint.com/186860/3d-printed-building-copenhagen/

4. Wu P, Wang J, Wang X. A critical review of the use of 3-D printing in the construction industry. Autom Constr. 2016 Aug 1;68(Supplement C):21–31.

5. Zocca A, Colombo P, Gomes CM, Günster J. Additive Manufacturing of Ceramics: Issues, Potentialities, and Opportunities. J Am Ceram Soc. 2015 Jul 1;98(7):1983–2001.

6. Woollaston V. The race to build the first 3D-printed building [Internet]. WIRED UK. [cited 2018 Apr 9]. Available from: http://www.wired.co.uk/article/architecture-and-3d-printing

7. World's first 3D-printed apartment building constructed in China [Internet]. CNET. [cited 2018 Apr 9]. Available from: https://www.cnet.com/news/worlds-first-3d-printed-apartment-building-constructed-in-china/

8. Europe's first 3D-printed building has been completed [Internet]. Building Design + Construction. [cited 2018 Apr 9]. Available from: https://www.bdcnetwork.com/europe%E2%80%99s-first-3d-printed-building-has-been-completed

9. Lim S, Buswell RA, Valentine PJ, Piker D, Austin SA, De Kestelier X. Modelling curved-layered printing paths for fabricating large-scale construction components. Addit Manuf. 2016 Oct 1;12(Part B):216–30.

10. Lim S, Buswell RA, Le TT, Austin SA, Gibb AGF, Thorpe T. Developments in construction-scale additive manufacturing processes. Autom Constr. 2012 Jan 1;21(Supplement C):262–8.

11. Wangler T, Lloret E, Reiter L, Hack N, Gramazio F, Kohler M, et al. Digital concrete: opportunities and challenges. RILEM Tech Lett. 2016;1:67–75.

12. Lowke D, Dini E, Perrot A, Weger D, Gehlen C, Dillenburger B. Particle-bed 3D printing in concrete construction – Possibilities and challenges. Cem Concr Res. 2018 Oct 1;112:50–65.

13. Xia M, Sanjayan J. Method of formulating geopolymer for 3D printing for construction applications. Mater Des. 2016 Nov 15;110(Supplement C):382–90.

14. Khoshnevis B. Automated construction by contour crafting—related robotics and information technologies. Autom Constr. 2004 Jan 1;13(1):5–19.

15. Paul SC, Tay YWD, Panda B, Tan MJ. Fresh and hardened properties of 3D printable cementitious materials for building and construction. Arch Civ Mech Eng. 2018 Jan 1;18(1):311–9.

16. Ma G, Li Z, Wang L. Printable properties of cementitious material containing copper tailings for extrusion based 3D printing. Constr Build Mater. 2018 Feb 20;162:613–27.

17. Buswell RA, Soar RC, Gibb AGF, Thorpe A. Freeform Construction: Mega-scale Rapid Manufacturing for construction. Autom Constr. 2007 Mar 1;16(2):224–31.

18. Le TT, Austin SA, Lim S, Buswell RA, Gibb AGF, Thorpe T. Mix design and fresh properties for high-performance printing concrete. Mater Struct. 2012 Aug 1;45(8):1221–32.

19. Hambach M, Volkmer D. Properties of 3D-printed fiber-reinforced Portland cement paste. Cem Concr Compos. 2017 May 1;79:62–70.

20. Perrot A, Rangeard D, Pierre A. Structural built-up of cement-based materials used for 3D-printing extrusion techniques. Mater Struct. 2016 Apr 1;49(4):1213–20.

21. Biernacki JJ, Bullard JW, Sant G, Brown K, Glasser FP, Jones S, et al. Cements in the 21st century: Challenges, perspectives, and opportunities. J Am Ceram Soc. 2017 Jul 1;100(7):2746–73.

22. Nair SA, Alghamdi H, Arora A, Mehdipour I, Sant G, Neithalath N. Linking fresh paste microstructure, rheology and extrusion characteristics of cementitious binders for 3D printing. J Am Ceram Soc. 2019;102(7):3951–3964.

23. Ness C, Ooi JY, Sun J, Marigo M, McGuire P, Xu H, et al. Linking particle properties to dense suspension extrusion flow characteristics using discrete element simulations. AIChE J. 2017 Jul 1;63(7):3069–82.

24. Benbow JJ, Bridgwater J. Paste flow and extrusion. Clarendon Press, Oxford, UK; 1993. 153 p.

25. Benbow JJ, Oxley EW, Bridgwater J. The extrusion mechanics of pastes—the influence of paste formulation on extrusion parameters. Chem Eng Sci. 1987;42(9):2151–2162.

26. Rough SL, Wilson DI, Bridgwater J. A model describing liquid phase migration within an extruding microcrystalline cellulose paste. Chem Eng Res Des. 2002;80(7):701–714.

27. Li M, Tang L, Landers RG, Leu MC. Extrusion Process Modeling for Aqueous-Based Ceramic Pastes—Part 1: Constitutive Model. J Manuf Sci Eng. 2013 Sep 11;135(5):051008-051008–7.

28. Patel MJ, Blackburn S, Wilson DI. Modelling of paste ram extrusion subject to liquid phase migration and wall friction. Chem Eng Sci. 2017 Nov 23;172:487–502.

29. Zhou X, Li Z. Numerical simulation of ram extrusion in short-fiber-reinforced fresh cementitious composites. J Mech Mater Struct. 2009;4:1755–1769.

30. Aydin I, Biglari FR, Briscoe BJ, Lawrence CJ, Adams MJ. Physical and numerical modelling of ram extrusion of paste materials: conical die entry case. Comput Mater Sci. 2000;18(2):141–155.

31. Khelifi H, Perrot A, Lecompte T, Rangeard D, Ausias G. Prediction of extrusion load and liquid phase filtration during ram extrusion of high solid volume fraction pastes. Powder Technol. 2013 Nov 1;249:258–68.

32. Vance K, Sant G, Neithalath N. The rheology of cementitious suspensions: A closer look at experimental parameters and property determination using common rheological models. Cem Concr Compos. 2015 May 1;59(Supplement C):38–48.

33. Vance K, Kumar A, Sant G, Neithalath N. The rheological properties of ternary binders containing Portland cement, limestone, and metakaolin or fly ash. Cem Concr Res. 2013 Oct 1;52(Supplement C):196–207.

34. Vance K, Arora A, Sant G, Neithalath N. Rheological evaluations of interground and blended cement–limestone suspensions. Constr Build Mater. 2015 Mar 15;79(Supplement C):65–72.

35. Neto C, Campiteli V. The Influence of Limestone Additions on the Rheological Properties and Water Retention Value of Portland Cement Slurries. In: Klieger P, Hooton R, editors. Carbonate Additions to Cement. 100 Barr Harbor Drive, PO Box C700, West Conshohocken, PA 19428-2959: ASTM International; 1990. p. 24–9.

36. Flatt RJ, Bowen P. Yodel: A Yield Stress Model for Suspensions. J Am Ceram Soc. 2006 Apr;89(4):1244–56.

37. Zhou Z, Solomon MJ, Scales PJ, Boger DV. The yield stress of concentrated flocculated suspensions of size distributed particles. J Rheol. 1999 Apr 26;43(3):651–71.

38. Saha PK. Aluminum Extrusion Technology. Available from: https://app.knovel.com/hotlink/toc/id:kpAET00001/aluminum-extrusion-technology/aluminum-extrusion-technology

39. Bagley E. End corrections in the capillary flow of polyethylene. J Appl Phys. 1957;28(5):624–627.

40. Liu H, Liu J, Leu MC, Landers R, Huang T. Factors influencing paste extrusion pressure and liquid content of extrudate in freeze-form extrusion fabrication. Int J Adv Manuf Technol. 2013 Jul;67(1–4):899–906.

41. Bayfield M, Haggett JA, Williamson MJ, Wilson DI, Zargar A. Liquid Phase Migration in the Extrusion of Icing Sugar Pastes. Food Bioprod Process. 1998 Mar 1;76(1):39–46.

42. Alghamdi H, Nair SA, Neithalath N. Insights into material design, extrusion rheology, and properties of 3D-printable alkali-activated fly ash-based binders. Mater Des. 2019;167:107634.

43. Toutou Z, Roussel N, Lanos C. The squeezing test: a tool to identify firm cement-based material's rheological behaviour and evaluate their extrusion ability. Cem Concr Res. 2005 Oct 1;35(10):1891–9.

44. Li Z, Li X. Squeeze flow of viscoplastic cement-based extrudate. J Eng Mech. 2007;133(9):1003–1008.

45. Banfill PFG. Rheology of fresh cement and concrete. Rheol Rev. 2006;2006:61.

46. Beakawi Al-Hashemi HM, Baghabra Al-Amoudi OS. A review on the angle of repose of granular materials. Powder Technol. 2018 May;330:397–417.

47. Paydar MH, Reihanian M, Ebrahimi R, Dean TA, Moshksar MM. An upper-bound approach for equal channel angular extrusion with circular cross-section. J Mater Process Technol. 2008 Mar 3;198(1):48–53.

48. Misiolek WZ. Material physical response in the extrusion process. J Mater Process Technol. 1996 Jun 15;60(1):117–24.

49. Tay YWD, Li MY, Tan MJ. Effect of printing parameters in 3D concrete printing: Printing region and support structures. J Mater Process Technol. 2019 Sep 1;271:261–70.

50. Alghamdi H, Neithalath N. Synthesis and characterization of 3D-printable geopolymeric foams for thermally efficient building envelope materials. Cem Concr Compos. 2019 Nov 1;104:103377.